



Zhao, H. et al. (2022) Gold-viral particle identification by deep learning in wide-field photon scattering parametric images. *Applied Optics*, 61(2), pp. 543-553. (doi: [10.1364/AO.445953](https://doi.org/10.1364/AO.445953))

The material cannot be used for any other purpose without further permission of the publisher and is for private use only.

There may be differences between this version and the published version. You are advised to consult the publisher's version if you wish to cite from it.

<https://eprints.gla.ac.uk/260566/>

Deposited on 13 December 2021

Enlighten – Research publications by members of the University of
Glasgow

<http://eprints.gla.ac.uk>

Gold-viral particle identification by deep learning in wide-field photon scattering parametric images

HANWEN ZHAO,^{1,8} BIN NI,^{1,8} XIAO JIN,¹ HENG ZHANG,¹ JAMIE JIANGMIN HOU,² LIANPING HOU,³ JOHN H. MARSH,³ LEI DONG,⁴ SHANHU LI,⁵ XIAOHONG W. GAO,⁶ DAMING SHI,⁷ XUEFENG LIU,^{1,9} AND JICHUAN XIONG,^{1,10}

¹*School of Electronic and Optical Engineering, Nanjing University of Science and Technology, Nanjing*

²*The Royal College of Surgeons of Edinburgh, Nicolson Street, Edinburgh, Scotland, UK EH8 9DW*

³*James Watt School of Engineering, University of Glasgow, Glasgow, G12 8QQ, UK*

⁴*School of Life Science, Beijing Institute of Technology, Beijing 100081, China*

⁵*Department of Cell Engineering, Beijing Institute of Biotechnology, Beijing, 100850, P. R. China*

⁶*Department of Computer Science, Middlesex University, London NW4 4BT, UK*

⁷*College of Computer Science and Software Engineering, Shenzhen University, China*

⁸*These authors contributed equally to this work*

⁹*liuxf_1956@sina.com*

¹⁰*Jichuan.xiong@njjust.edu.cn*

Abstract: The ability to identify virus particles is important for research and clinical applications. Because of the optical diffraction limit, conventional optical microscopes are generally not suitable for virus particle detection, and higher resolution instruments such as transmission electron microscopy (TEM) and scanning electron microscopy (SEM) are required. In this paper, we propose a new method for identifying virus particles based on polarization parametric indirect microscopic imaging (PIMI) and deep learning techniques. By introducing an abrupt change of refractivity at the virus particle using antibody-conjugated gold nanoparticles (AuNPs), the strength of the photon scattering signal can be magnified. After acquiring the PIMI images, a deep learning method was applied to identify discriminating features and classify the virus particles, using electron microscopy (EM) images as the ground truth. Experimental results confirm that gold-virus particles can be identified in PIMI images with a high level of confidence.

© 2021 Optica Publishing Group

1. Introduction

There is a need for techniques that can be widely deployed and used to identify virus rapidly, a need has been reinforced since 2020 by the COVID-19 pandemic [1]. Traditional chemical techniques [2-4] are slow and transmission electron microscopy (TEM) [5-8] is not suitable to widespread deployment outside laboratories. Optical sensing methods [9,10], however, can be more convenient and economical, which are promising to offer a fine solution.

In optical methods, the key challenge for virus detection is to develop an experimental configuration that can detect and isolate the smallest possible signal efficiently. This challenge is being solved through various efforts to reduce the imaging background or amplify the target signal. In terms of label-free virus detection, interferometric scattering microscopy (iSCAT) has proved to have capability to detect a single virus. Initial studies reported the label-free optical

detection of single virus particle bound to the supported membrane bilayer receptors [11,12]. Manoharan et al. also tracked the position and orientation of label-free bacteriophages and monitored the changes in iSCAT contrast as a function of viral DNA content [13]. The same group quantified the assembly kinetics of individual MS2 bacteriophage capsids around MS2 RNA, and identified the characteristics of capsid growth [14]. In terms of amplifying viral signal, current optical methods are mainly based on measurements of the localized surface plasmon resonance (LSPR) spectrum from AuNP labeled virus. The AuNPs are used as functionalized labels to enhance the wavelength shift of the LSPR spectrum, so the sensitivity depends on the intensity of the plasmonic emission. Nonspecific binding of AuNPs to other components in the heterogeneous medium and the formation of aggregates remain a challenge, along with the instability of the fluorescent signal which depends on the size of the biological nanoparticle. However, images of plasmonic emission from virus-AuNPs complexes carry a wealth of information and can in principle be used for highly sensitive virus detection.

In our previous work, we have investigated the ability of polarization indirect microscopic imaging (PIMI) to resolve nano-features and molecular structures from the spatial polarization status distribution in the nano scattering field [15-18]. We also demonstrated that anisotropy in nanostructures can be identified from the scattered photon distribution [19,20]. Moreover, the PIMI scattering strength of viruses can be magnified by introducing an abrupt change of refractivity at the virus particle, enhancing the signal to the point where the presence of virus can be identified [21].

Accurate processing and analysis of PIMI spectra is an important part for obtaining information regarding the structural feature of viruses. There are many algorithms for identifying and analyzing small objects in optical microscopy images. Ronneberger et al. used the active contour method to segment pollen grains in a brightfield microscope image [22]. Ranzato et al. proposed a system that can actively recognize biological particles in microscopic images [23]. Oktay et al. utilized a convolutional neural network with multiple output to achieve automatic detection, localization and segmentation of nanoparticles [24].

Owing to the presence of noise, the manual identification of viral particles in PIMI images is very time-consuming and has high error rate. Systematic noise significantly degrades the image resolution and contrast, which is mainly due to mechanical and electrical disturbances associated with modulation of the illumination when acquiring raw images. Deep learning can eliminate noise interference, and has good robustness and generalization abilities, so it is widely used in particle recognition tasks. Ito et al. and Xiao et al. employed different neural network models to achieve virus particle recognition in TEM images [25, 26]. Kolenov et al. applied a convolutional neural network to classify nanoparticles by using coherent scatterometry data [27]. Okunev et al. proposed a nanoparticle recognition method for scanning probe microscopy images by combining computer vision and deep learning techniques [28]. In the wider field of object detection and recognition, deep learning methods have achieved detection results with high accuracy [29-31].

Because of the convenience and cost-effectiveness of optical methods for virus detection, in this paper we propose a method based on the combination of PIMI and deep learning. Our methodology is as follows: firstly, viruses are labeled with a AuNP-hexon complex (AuNP-hAb) probe to turn the virus into gold-viral particles. Then, all samples are imaged by the Scanning Electron Microscope (SEM), TEM and PIMI methods. The TEM and SEM images are taken as the ground truth, and by comparing the corresponding images of particles in the PIMI and SEM/TEM images we can teach the deep learning algorithm to identify different types and orientations of gold-viral complexes. The Faster R-CNN [32] is then used to identify the type of particles in the PIMI images. The experimental results demonstrated that our method can be used to identify gold-viral particle with high accuracy and therefore provides a new optical method for virus detection.

2. Materials and methods

2.1 Virus labeled by AuNP-hexon complex (AuNP-hAb) probe and EM data

In the experiments reported here, adenovirus was used as the virus sample for detection. Adenovirus is a type of icosahedral virus that can infect the respiratory tract, gastrointestinal tract, urethra, bladder, eyes and liver. Neutralizing antibody (Ab) responses to adenovirus are directed at components of the virion surface, primarily against fiber, penton base, and hexon proteins. Fiber and penton-based proteins present at the vertices of the capsid are involved in cell attachment and entry. Hexon, the major component of the icosahedral virus particle, comprises the facets of virion and constitutes the bulk of icosahedral capsid [33]. It was expected that the AuNP-hAb probes would attach to the virus in positions corresponding to the recognition site.

The adenovirus was purchased from Hanbio Biological Technology Co. Ltd. Rabbit anti-Adenovirus hexon protein antibody (hAb) was purchased from Beijing Biosynthesis Biotechnology Co. Ltd. (catalog number: bs-12354R). $\text{HAuCl}_4 \cdot 3\text{H}_2\text{O}$ was purchased from Sigma-Aldrich Co. Ltd. Other reagents were purchased from Sinopharm Group Chemical Reagent Co. Ltd. All commercially available reagents were used directly without any further purification. In all experiments, deionized Millipore water ($18.25 \text{ M}\Omega \text{ cm}$) was used.

To modify the surface of gold with antibodies, we prepared multilayer AuNP-polyelectrolyte nanoparticles using a layer-by-layer assembly approach which involved sequentially coating negatively charged polystyrene sulfonate (PSS) onto the AuNP-CTAB (cetyltrimethylammonium bromide). The detailed process was described in [34]. Measurement of the particle size distribution showed that the synthesized AuNP-CTAB has a mean diameter of $84.7 \pm 0.3 \text{ nm}$. It is worth noting that different polymers on the surface of the AuNPs did not cause any change in the macroscopic morphology (data not shown here). The zeta potential of AuNP-CTAB ($+26.9 \pm 0.9 \text{ mV}$) flipped from positive to negative, further confirming the successful surface passivation of AuNP-PSS ($-45.4 \pm 2.6 \text{ mV}$). The surface charge resulted in repulsion and ensured a homogenous dispersion of AuNPs.

The antibodies were thought to be conjugated to the AuNP-PSS by a mechanism similar to the binding of antibodies to nanospheres, i.e., through an electrostatic physisorption interaction [35]. Next, the prepared AuNP-hAb probes were used to capture the adenovirus. Finally, three different particles were present in the same sample: single AuNPs (antibody-conjugated gold nanoparticle), double AuNPs and gold-virus (AuNP-virus).

The ground truth in our experiments was composed of TEM and SEM images. In order to associate these with particles in the PIMI image, each EM image was annotated as shown in Fig. 1. Each sample contained 10 to 30 gold-virus particles and was imaged using a TEM (JEM-2100, Japan) with an acceleration voltage of 200 kV and an SEM, (JSM-IT500HR).

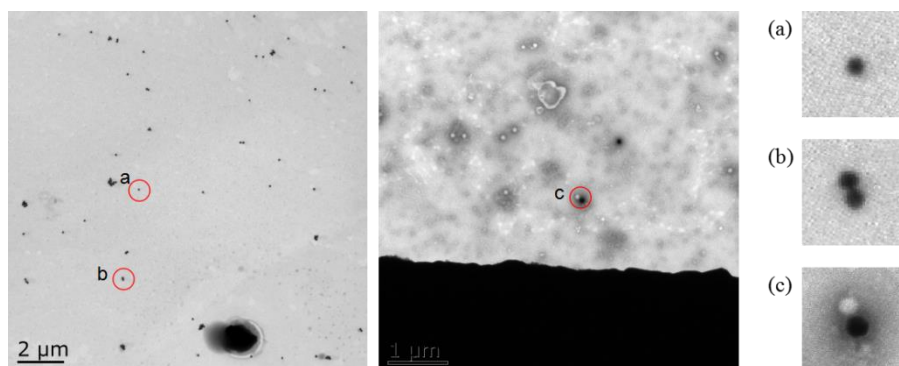


Fig. 1. Comparison of TEM images for different structures. (a) single AuNPs, (b) double AuNPs and (c) AuNP-virus. The images on the right are the enlarged images of the corresponding positions on the left.

2.2 PIMI data and pre-processing

The proposed system for identifying gold-virus particles is shown in Fig. 2. PIMI is a far-field indirect imaging technique that can resolve anisotropic features in samples with high resolution and contrast. PIMI obtains anisotropic nanoscale structural information about the sample by utilizing a polarization modulated illumination scheme and analyzing the far-field variation of polarization states of the scattered photons. By fitting and filtering the intensity variations of the image pixels, a set of parametric images, such as $\sin(\delta)$ and Φ images, can be obtained in which the spatial resolution is greatly enhanced compared to conventional optical microscopy, enabling the collection of features smaller than 100 nm [18].

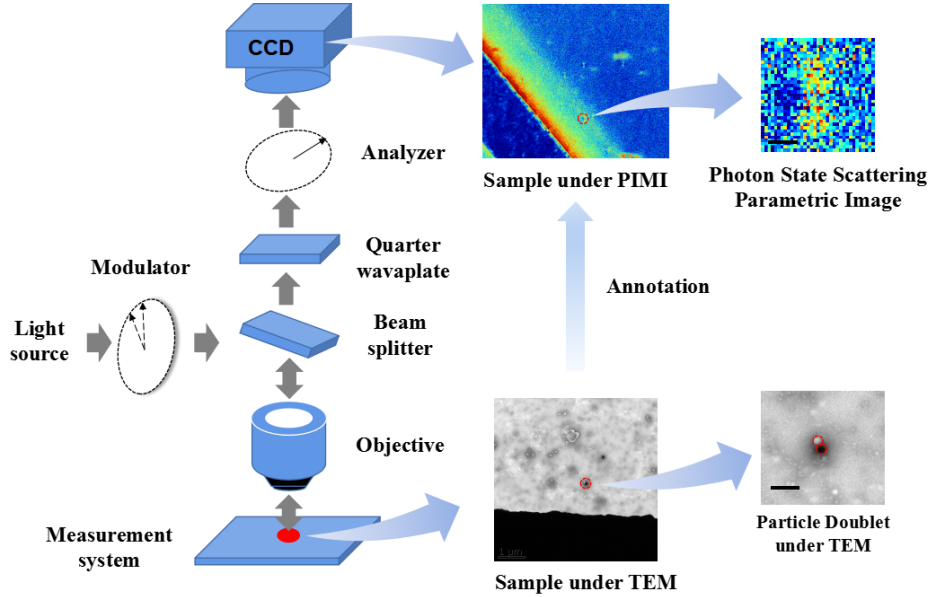


Fig. 2. System and process of obtaining the data set using the annotated EM data to classify each particle in the PIMI image.

As shown in Fig. 2, an Olympus reflection microscopic system (BX51M) was used to provide the basic optical path. A 532 nm filter with its FWHM of 10 nm and a polarizer were inserted after the light source, so that rotating polarized light could be produced. The light source is illuminated by a mercury lamp with a broad band. A quarter wave plate and a high extinction-ratio polarizer were inserted in the beam path between the objective lens and imaging sensor, and the fast axis is oriented at 45° and 90° respectively to the plane of the paper. The numerical aperture (NA) for the objective is 0.9, with magnification of 100X, and the working medium is air. The imaging sensor is a monochromatic visible light CCD camera manufactured by Basler (piA2400-17gm) with a pixel size of $3.45 \mu\text{m} \times 3.45 \mu\text{m}$. When coupled with 100X objective, the image pixel size will be $34.5 \text{ nm} \times 34.5 \text{ nm}$. The overall field-of-view is controlled by the CCD size of 1836×1537 pixels, which is about $63 \mu\text{m} \times 53 \mu\text{m}$ under 100X objective.

An unprocessed $\sin(\delta)$ PIMI image is shown in Fig. 3, where the red circles represent single AuNPs, blue circles represent double AuNPs and yellow circles represent possible AuNP-virus doublets. The enlarged PIMI $\sin(\delta)$ and SEM images for the aforementioned three kinds of particles are also shown in Fig. 3. The dataset in our experiments was composed of 6 PIMI images taken from six samples. The number of gold particles in each image ranged from 20 to 60 and each sample contained 10 to 30 gold-virus particles. The size of every PIMI image used in the experiments was 1836×1537 pixels. By taking the TEM images of all particles as a reference, we could label the particle at the corresponding position in the PIMI images. Each image was cropped to 320×320 pixels to reduce the computational time for image processing and training of the neural network model.

2.3 Neural Network

The neural network used in our work was the Faster R-CNN [31]. The structure of the network is shown in Fig. 4. The network is divided into four parts: convolutional layers (VGG16), Region Proposal Network (RPN), Region of Interest (ROI) pooling and classifier. The pre-trained VGG16 is used as the feature extractor of the network and generates 512 feature maps (20×20 in size) of input image. RPN first generates 9 anchor boxes for each point on the feature map and two branches appear. One of the branches reshapes and filters all the anchor boxes ($20 \times 20 \times 9$ in total) and predicts that the anchors belong to the foreground or the background through softmax; at the same time, the other branch modifies the position of anchor boxes to form a more accurate proposal. Next, through the threshold operation, three hundred optimal region proposal boxes are selected. The input of ROI pooling are the region proposal boxes generated by the RPN and the feature map generated by the last layer of VGG16. Through the mapping of the feature maps, a total of 300×512 regions can be obtained. Then these regions are divided into 7×7 . For each block, we use the max pooling method to select the pixel with the maximum value as the output, so that a 7×7 feature map is formed. Finally, 300×512 feature maps are used as the input of the fully connected layer, and accurate region box prediction and classification are calculated.

The network was fine-tuned for 60000 epochs with a learning rate of 0.001 in epochs 0–53999 and 0.0001 in 54000–60000 epochs. The cropped 320×320 resolution PIMI images were used for training by adjusting the max_size parameter of the config file to the required image size. Training and identification were carried out on a NVIDIA Tesla V-100 32 GB GPU machine with the Tensorflow framework. The flow of our neural network method is described in Fig. 5. The training process is based on the original PIMI image. The annotated EM image acts as a ground truth to produce the annotated PIMI image. Based on the original PIMI image, the annotated PIMI image and the Faster R-CNN techniques, gold-viral particle identification from the tested PIMI image can be achieved with high accuracy.

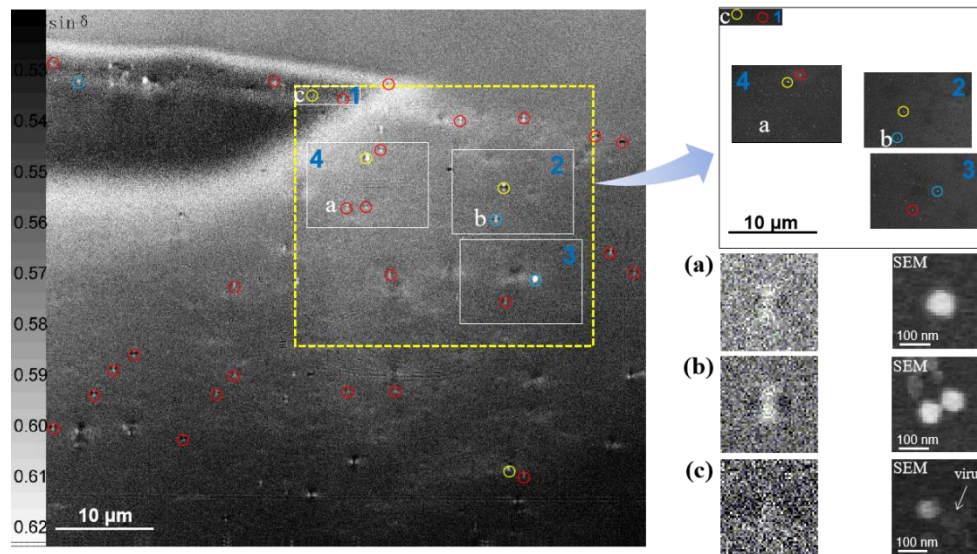


Fig. 3. Comparison of images of different structures. (a) single AuNPs, (b) double AuNPs and (c) AuNP-virus. Left part is the PIMI $\sin(\delta)$ image of the whole field (red circle represents single AuNPs, blue circle represents double AuNPs and yellow circle represents possible AuNP-virus doublet), top right are the correspondent SEM images of rectangular regions in the left PIMI image, bottom right are the enlarged PIMI $\sin(\delta)$ (left) and SEM (right) images of three kinds of structures.

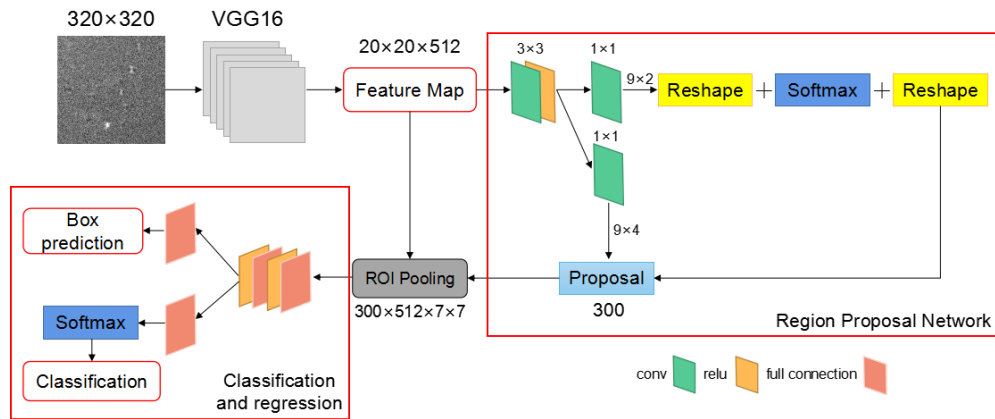


Fig. 4. Faster R-CNN architecture

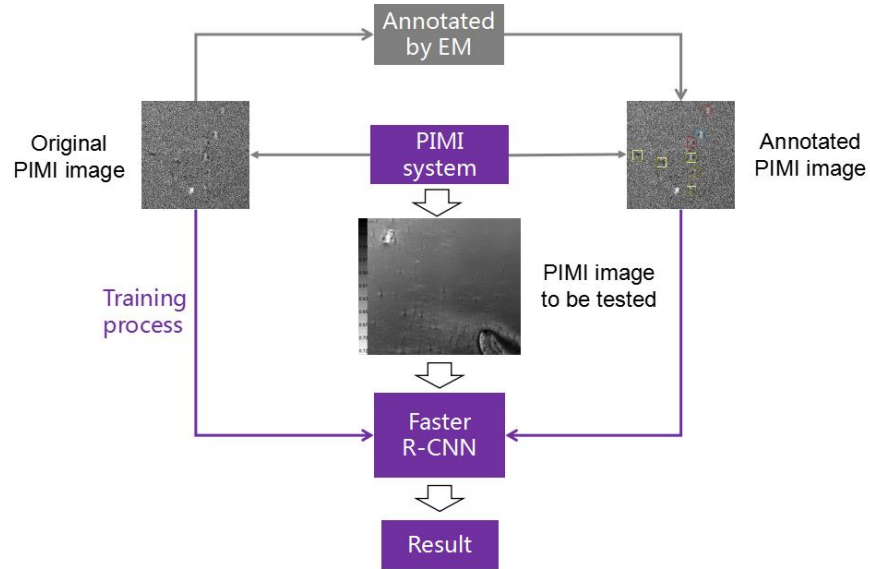


Fig. 5. Experiment flow chart

3. Results and discussion

3.1 Detection of gold-viral particles by scattering spectrum

Under normal circumstances, we detected virus particles by analyzing the scattering spectrum of PIMI, as shown in Fig. 6. To compare the scattering spectra and characteristic curves, we used finite difference time domain (FDTD) software to simulate the PIMI images. The simulation was based on FDTD solutions of Maxwell's equations. Here we simulated the electric field of AuNPs excited by polarized light. The structure comprised a $4\ \mu\text{m}$ (length) \times $4\ \mu\text{m}$ (width) \times $30\ \text{nm}$ (height) carbon film substrate and single or double AuNPs with a diameter of $80\ \text{nm}$ lying at the center of the substrate surface. A conjugated structure consisting of a sphere, with its diameter and refractive index of $80\ \text{nm}$ and 1.47 , and a spherical AuNP with its diameter of $100\ \text{nm}$ was used to model gold-virus doublet. A total-field scattered-field (TFSF) source with a wavelength of $532\ \text{nm}$ was placed above the AuNP and the virus samples. The polarization angle was increased in steps of 18° and the data for polarization angles (relative to the x -axis) from 0° to 162° at a particular height were collected. The initial data set therefore

consisted of ten ($162/18+1=10$) images from which the PIMI images were then calculated.

A method based on self-similarity-encoded deep learning was applied to experimental PIMI images. We used 16 layers of random code Z as the input to a U-shaped generating network and the parametric images with noise were mapped directly through the network. The gradient descent algorithm was used to obtain the optimal network parameters without the need for a ground truth. After a certain number of learning epochs, we used the network's priori and self-similarity of the parametric image to reduce the noise and improve the resolution of the experimental PIMI images.

The first column of (a), (b) and (c) display PIMI $\sin(\delta)$ images of AuNPs, double AuNPs and AuNP-virus, respectively. The graphs in the second column are scans of position along the red dotted line in the images in the first column, and the blue line and red line indicate experimental data and FDTD data respectively. The value of the abscissa indicates the position on the dotted line in the figure (from left to right), and the range is from 0 to 1200 nm. The ordinate represents the value of $\sin(\delta)$. The first row presents raw images that are almost overwhelmed by noise. Therefore, we denoised the original image to obtain much improved images, as shown in the second row. For comparison, we used FDTD to simulate the PIMI images of the recorded objects, as shown in the last row.

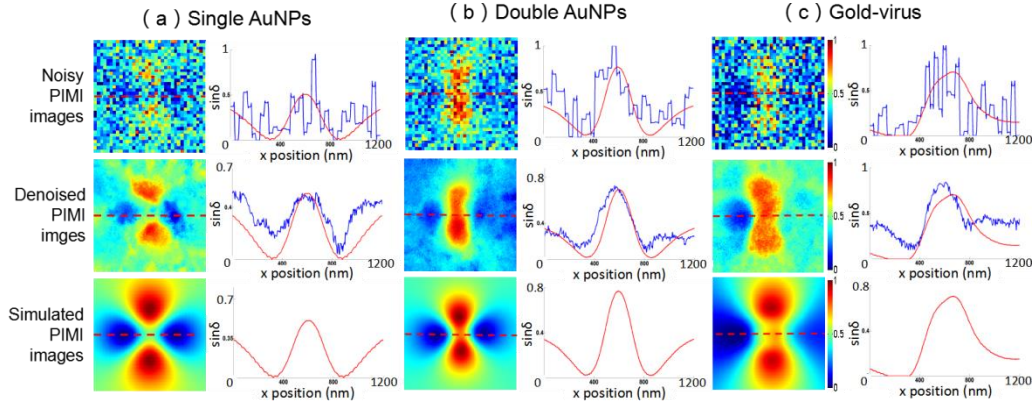


Fig. 6. PIMI $\sin(\delta)$ images, denoised PIMI $\sin(\delta)$ images, simulated PIMI $\sin(\delta)$ images and their characteristic curves: (a) single AuNPs, (b) double AuNPs, (c) gold-virus. The blue line and red line indicate experimental data and simulated data, respectively.

By comparing the characteristic curves of the three particles, we can find that the scattering spectra of the three particles have different characteristics. In the denoised PIMI $\sin(\delta)$ image, the symmetry of the scattering dipoles of the AuNPs are significantly modified by the combination of virus to the AuNPs, and the FDTD image confirms this. Using the symmetry, asymmetry and intensity of the scattering spectrum, it is possible to identify gold-viral particles. However, in many unexpected situations, the interference of noise seriously affects the process of identification; even after denoising, the detection accuracy cannot be improved. Because of such issue, we need to use a deep learning technique to enhance the detection accuracy of gold-viral particle complexes.

3.2 Detection of gold-viral particles by deep learning

To analyze the reliability of the proposed method, we divided the data set into a training set and a test set. After 60000 iterations of learning, we used PIMI images as the test set to input into the network. The identification results are shown in Fig. 7. As we can see, the three different particle types have been detected and recognized. The pictures in the left column are the identification results for single AuNPs. We find that the PIMI scattering state of single AuNPs is relatively consistent. The images in the middle and the right are the recognition results of

double AuNPs and AuNP-virus respectively. Compared with single AuNPs, their scattering states take many forms which are very difficult to distinguish by the naked eye. We will report in-depth studies of these multiple scattering states in our future work.

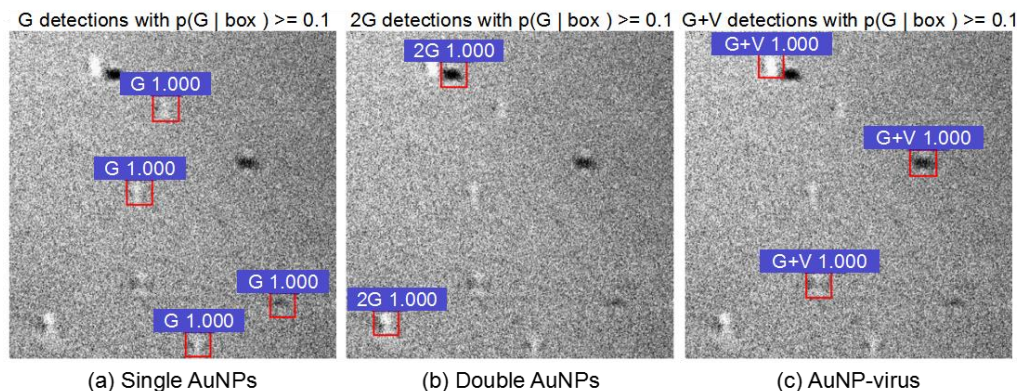


Fig. 7. Gold-viral particle identification results: (a), (b) and (c) represent the PIMI images of single AuNPs, double AuNPs and AuNP-virus respectively. The first half of the text in the blue boxes represents the category, and the second half is the probability.

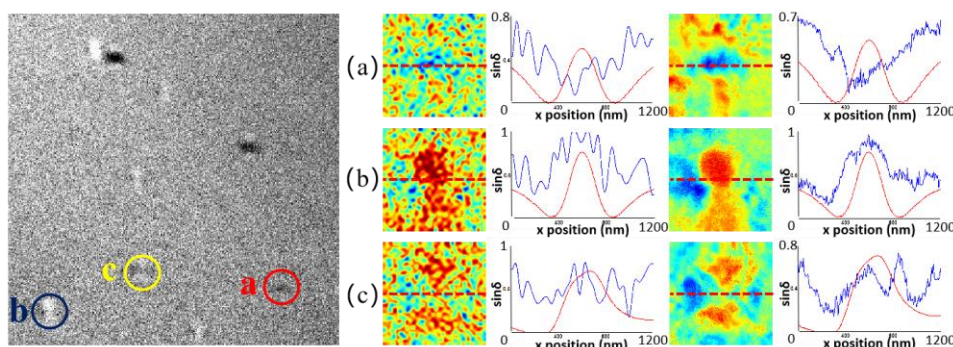


Fig. 8. Spectral analysis results of gold-virus identification: (a) Single AuNPs, (b) Double AuNPs, (c) gold-virus. The blue line and red line indicate experimental data and simulated data, respectively.

For comparison, we used the characteristic curve method to analyze regions in the deep learning results, as shown in the right part of Fig. 8. Figs. 8(a), 8(b) and 8(c) illustrate the extracted results from the corresponding areas in the left picture. The images in the first column and the third column represent the original $\sin(\delta)$ image and the denoised result, respectively. Similarly, the graphs in the second column and fourth column are based on positions along the red dotted lines in the left column images. The blue and red solid lines indicate experimental data and FDTD data respectively. As we can see, the original PIMI image is severely degraded by noise, so the characteristic curve is also distorted. Even after denoising, the situation is not notably improved, as shown in the images in the third and fourth columns. The denoised curve does not match the simulated curve, so method of analysis is unable to distinguish the three types of particles. Therefore, for cases with high noise, the method of spectral analysis is ineffective in identifying the gold-virus complexes.

All the pictures in the test set were then analyzed using the deep learning algorithm and the results are summarized in Table 1. The positive identification of single AuNPs and gold-virus complexes show high accuracy. The overall accuracy rate reached 93.54%, and for AuNP-virus, the identification rate reached 94.44%. However, the identification accuracy for double AuNPs is comparatively low, only 81%. In order to see which particle the network struggles to

distinguish and to what degree, we built the confusion matrix in Fig. 9. The horizontal axis represents the particle types predicted by the network, and the vertical axis represents the true particle labels. One can see that, single AuNPs and gold-virus are difficult to confuse with other particles. However, about one-fifth of double AuNPs is identified as single AuNPs and gold-virus, and the number is nearly half by half. This is to be expected, because the quantity of double AuNPs in the sample is very small, making it difficult for the neural network to learn all the characteristics of the scattering spectrum from double AuNPs. On the other hand, in many scenarios, the scattering spectrum of double AuNPs is similar to that of gold-virus, which may lead to an erroneous increase in the identification rate of gold-virus. This is now the direction of our effort to improve the overall detection accuracy.

Table 1. Identification performance of different particles in PIMI images.

class	Single AuNPs	Double AuNPs	AuNP-virus
Total	289	21	108
Positive sample	272	17	102
Accuracy	0.9412	0.8095	0.9444

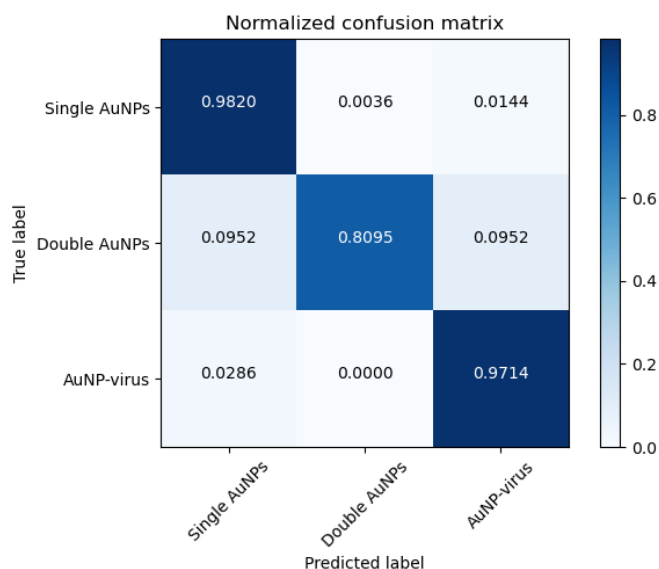


Fig. 9. Prediction accuracy of three particles in confusion matrix

4. Conclusion

In this work, we propose a new optical method to identify viruses based on PIMI and deep learning. By introducing AuNPs-hAb, the scattering spectrum structure of AuNPs and adenovirus are changed. The PIMI system can capture scattered signals that cannot be captured by traditional microscopes. By examining differences in the scattering spectra, we can identify gold-viral particles to a certain extent. In order to reduce noise interference and improve the virus detection efficiency, we used a deep learning method to learn the scattering characteristics of three types of particles. Based on TEM and SEM data, we created a ground truth data set, using which the deep learning algorithm demonstrated 94% accuracy when identifying gold-viral particle complexes. This technique has the potential to detect low concentrations of virus or even a single virus particle.

Acknowledgments

This work was supported by the National Major Scientific Instruments and Equipment Development Project [grant number 61827814], Beijing Natural Science Foundation [grant number Z190018], the National Natural Science Foundation of China [grant number 62105155], the Natural Science Foundation of Jiangsu Province [grant number BK20210326] and the Ministry of Education collaborative project [grant number B17023]. They also acknowledge support from the UK Engineering and Physical Sciences Research Council [grant number EP/R042578/1], and from the UK Royal Society [grant number IEC/NSFC/181557].

Disclosures

The authors declare no conflicts of interest.

Data Availability

Data underlying the results presented in this paper are not publicly available at this time but may be obtained from the authors upon reasonable request.

References

- [1] M. Mofijur, I. M. R. Fattah, M. A. Alam, A. B. M. S. Islam, H. C. Ong, S. M. A. Rahman, G. Najafi, S. F. Ahmed, M. A. Uddin, and T. M. I. Mahlia, "Impact of COVID-19 on the social, economic, environmental and energy domains: Lessons learnt from a global pandemic," *Sustain. Prod. Consump.* **26**, 343–359 (2021).
- [2] B. Chaharain, A. R. Omar, I. Aini, K. Yusoff, and S. S. Hassan, "Detection of H5, H7 and H9 subtypes of avian influenza viruses by multiplex reverse transcription-polymerase chain reaction," *Microbiol. Res.* **164**(2), 174–179 (2009).
- [3] J. Cui, F. Li, and Z. L. Shi, "Origin and evolution of pathogenic coronaviruses," *Nat. Rev. Microbiol.* **17**(3), 181–192 (2019).
- [4] Q. He, D. Yu, M. Bao, G. Korensky, J. Chen, M. Shin, J. Kim, M. Park, P. Qin, and K. Du, "High-throughput and all-solution phase African Swine Fever Virus (ASFV) detection using CRISPR-Cas12a and fluorescence based point-of-care system," *Biosens. Bioelectron.* **154**, 112068 (2020).
- [5] M. Nermut, and A. Steven, "Animal Virus Structure," vol. 3, Elsevier, 1987.
- [6] Z. Wen, Z. Li, Y. Peng, and S. Ying, "Virus image classification using multi-scale completed local binary pattern features extracted from filtered images by multi-scale principal component analysis," *Pattern Recognit. Lett.* **79**, 25–30 (2016).
- [7] G. Kylberg, M. Uppström, K. Hedlund, G. Borgefors, and I. Sintorn, "Segmentation of virus particle candidates in transmission electron microscopy images," *J. Microsc.* **245**(2), 140–147 (2012).
- [8] I. Sintorn, M. Homman-Loudiyi, C. Söderberg-Nauclér, and G. Borgefors, "A refined circular template matching method for classification of human cytomegalovirus capsids in TEM images," *Comput. Methods Programs Biomed.* **76**(2), 95–102 (2004).
- [9] K. Niikura, K. Nagakawa, N. Ohtake, T. Suzuki, Y. Matsuo, H. Sawa, and K. Ijiro, "Gold nanoparticle arrangement on viral particles through carbohydrate recognition: A non-cross-linking approach to optical virus detection," *Bioconjugate Chem.* **20**(10), 1848–1852 (2009).
- [10] Y. T. Yeh, K. Gulino, Y. Zhang, A. Sabestien, T. W. Chou, B. Zhou, Z. Lin, I. Albert, H. Lu, V. Swaminathan, E. Ghedin, and M. Terrones, "A rapid and label-free platform for virus capture and identification from clinical samples," *Proc. Natl. Acad. Sci. U. S. A.* **117**, 895–901 (2020).
- [11] P. Kukura, H. Ewers, C. Müller, A. Renn, A. Helenius, and V. Sandoghdar, "High-Speed Nanoscopic Tracking of the Position and Orientation of a Single Virus," *Nat. Methods* **6**, 923–927 (2009).
- [12] H. Ewers, V. Jacobsen, E. Klotzsch, A. E. Smith, A. Helenius, and V. Sandoghdar, "Label-Free Optical Detection and Tracking of Single Virions Bound to Their Receptors in Supported Membrane Bilayers," *Nano Lett.* **7**, 2263–2266 (2007).
- [13] A. M. Goldfain, R. F. Garmann, Y. Jin, Y. Lahini, and V. N. Manoharan, "Dynamic Measurements of the Position, Orientation, and DNA Content of Individual Unlabeled Bacteriophages," *J. Phys. Chem. B.* **120**, 6130–6138 (2016).
- [14] R. F. Garmann, A. M. Goldfain, and V. N. Manoharan, "Measurements of the Self-Assembly Kinetics of Individual Viral Capsids around Their RNA Genome," *Proc. Natl. Acad. Sci. U. S. A.* **116**, 22485–22490 (2019).

- [15] K. Ullah, X. Liu, H. Muhammad, and Z. Shen, "Subwavelength far field imaging of nanoparticles with parametric indirect microscopic imaging," *ACS Photonics* **5**(4), 1388–1397 (2018).
- [16] G. Liu, K. Gao, X. Liu, and G. Ni, "Analysis on near field scattering spectra around nanoparticles by using parametric indirect microscopic imaging," *Opt. Commun.* **377**, 59–64 (2016).
- [17] K. Ullah, X. Liu, M. Habib, L. Song, N. Yadav, and B. Garcia-Camara, "Light scattering by subwavelength Cu₂O particles," *Nanotechnology* **28**(13), 134002 (2017).
- [18] W. Liu, J. Xiong, L. Zhu, S. Ye, H. Zhao, J. Liu, H. Zhang, L. Hou, J. H. Marsh, L. Dong, X. W. Gao, D. Shi, and X. Liu, "Characterization of deep sub-wavelength nanowells by imaging the photon state scattering spectra," *Opt. Express* **29**, 1221–1231 (2021).
- [19] K. Ullah, X. Liu, A. Krasnok, M. Habib, L. Song, and B. Garcia-Camara, "Resolving the multipolar scattering modes of a submicron particle using parametric indirect microscopic imaging," *Photonics Nanostruct. Fundam. Appl.* **30**, 7–13 (2018).
- [20] W. Liu, J. Xiong, H. Zhang, X. Liu, G. Liu, and H. Zhao, "Characterization of Komagataeibacter xylinus by a polarization modulation imaging method," *J. Phys. D: Appl. Phys.* **53**(12), 125403– (2020).
- [21] H. Zhang, X. Jin, H. Zhao, Y. Lin, X. Li, L. Hou, J. Marsh, L. Dong, D. Shi, W. Liu, B. Xu, B. Ni, J. Liu, J. Xiong, and X. Liu, "Photon Scattering Signal Amplification in Gold-Viral Particle Ligation Towards Fast Infection Screening," *IEEE Photonics J.* **13**(3), 1–11 (2021).
- [22] O. Ronneberger, Q. Wang, and H. Burkhardt, "Fast and robust segmentation of spherical particles in volumetric data sets from brightfield microscopy," in: *2008 5th IEEE International Symposium on Biomedical Imaging: From Nano to Macro*, 2008, pp. 372–375.
- [23] M. Ranzato, P. Taylor, J. House, R. Flagan, Y. LeCun, and P. Perona, "Automatic recognition of biological particles in microscopic images," *Pattern Recognit. Lett.* **28**(1), 31–39 (2007).
- [24] A. Oktay, and A. Gurses, "Automatic detection, localization and segmentation of nano-particles with deep learning in microscopy images," *Micron* **120**, 113–119 (2019).
- [25] E. Ito, T. Sato, D. Sano, E. Utagawa, and T. Kato, "Virus Particle Detection by Convolutional Neural Network in Transmission Electron Microscopy Images," *Food Environ. Virol.* **10**, 201–208 (2018).
- [26] C. Xiao, X. Chen, Q. Xie, G. Li, H. Xiao, J. Song, and H. Han, "Virus identification in electron microscopy images by residual mixed attention network," *Comput. Methods Programs Biomed.* **198**, 105766 (2021).
- [27] D. Kolenov, D. Davidse, J. Le Cam, and S. Pereira, "Convolutional neural network applied for nanoparticle classification using coherent scatterometry data," *Appl. Opt.* **59**, 8426–8433 (2020).
- [28] A. Okunev, M. Mashukov, A. Nartova, and A. Matveev, "Nanoparticle Recognition on Scanning Probe Microscopy Images Using Computer Vision and Deep Learning," *Nanomaterials* **10**(7), 1285 (2020).
- [29] R. Girshick, J. Donahue, T. Darrell, and J. Malik, "Rich feature hierarchies for accurate object detection and semantic segmentation," in: *Proceedings of the Conference on Computer Vision and Pattern Recognition (CVPR)*, IEEE, 2014, pp. 580–587.
- [30] J. Dai, Y. Li, K. He, and J. Sun, "R-FCN: Object Detection via Region-based Fully Convolutional Networks," in: *Proceedings of the Neural Information Processing Systems (NeurIPS)*, MIT Press, 2016, pp. 379–387.
- [31] J. Redmon, S. Divvala, R. Girshick, and A. Farhadi, "You Only Look Once: Unified, Real-Time Object Detection," in: *Proceedings of the Conference on Computer Vision and Pattern Recognition (CVPR)*, IEEE, 2016, pp. 779–788.
- [32] S. Ren, K. He, R. Girshick, and J. Sun, "Faster R-CNN: Towards Real-Time Object Detection with Region Proposal Networks," *IEEE Trans. Pattern Anal. Mach. Intell.* **39**(6), 1137–1149 (2017).
- [33] V. Reddy, and M. Barry, "Structural organization and protein-protein interactions in human adenovirus capsid," *Sub-Cell Biochem.* **96**, 503–518 (2021).
- [34] N. Azman, L. Bekale, T. Nguyen, and J. Kah, "Polyelectrolyte stiffness on gold nanorods mediates cell membrane damage," *Nanoscale* **12**(26), 14021–14036 (2020).
- [35] X. Huang, I. El-Sayed, W. Qian, and M. El-Sayed, "Cancer cell imaging and photothermal therapy in the near-infrared region by using gold nanorods," *J. Am. Chem. Soc.* **128**(6), 2115–2120 (2006).